Insights on the Formation Conditions of Uranus and Neptune from Their Deep Elemental Compositions

Olivier Mousis, Antoine Schneeberger, Thibault Cavalié, Kathleen E. Mandt, Artyom Aguichine, Jonathan I. Lunine, Tom Benest Couzinou, Vincent Hue, Raphaël Moreno

The Planetary Science Journal, 5:173 (15pp), 2024 August https://doi.org/10.3847/PSJ/ad58d8

Insights on the Formation Conditions of Uranus and Neptune from Their Deep Elemental Compositions

Olivier Mousis[1,2], Antoine Schneeberger[1], Thibault Cavalié[3,4], Kathleen E. Mandt[5], Artyom Aguichine[6], Jonathan I. Lunine[7], Tom Benest Couzinou[1], Vincent Hue[1], and Raphaël Moreno[4]
[1] Aix-Marseille Université, CNRS, CNES, Institut Origines, LAM, Marseille, France; olivier.mousis@lam.fr
[2] Institut Universitaire de France (IUF), France
[3] Laboratoire d'Astrophysique de Bordeaux, Univ. Bordeaux, CNRS, B18N, allée Geoffroy Saint-Hilaire, 33615, Pessac, France
[4] LESIA, Observatoire de Paris, Université PSL, CNRS, Sorbonne Université, Université Paris Cité, 5 place Jules Janssen, 92195 Meudon, France
[5] NASA Goddard Space Flight Center, Greenbelt, MD 20771, USA
[6] Department of Astronomy and Astrophysics, University of California, Santa Cruz, CA 95064, USA
[7] Department of Astronomy, Cornell University, Ithaca, NY 14850, USA
Received 2024 February 8; revised 2024 June 1; accepted 2024 June 14; published 2024 August 8

Abstract

This study, placed in the context of the preparation for the Uranus Orbiter Probe mission, aims to predict the bulk volatile compositions of Uranus and Neptune. Using a protoplanetary disk model, it examines the evolution of trace species through vapor and solid transport as dust and pebbles. Due to the high carbon abundance found in their envelopes, the two planets are postulated to have formed at the carbon monoxide ice line within the protosolar nebula. The time evolution of the abundances of the major volatile species at the location of the CO ice line is then calculated to derive the abundance ratios of the corresponding key elements, including the heavy noble gases, in the feeding zones of Uranus and Neptune. Supersolar metallicity in their envelopes likely results from accreting solids in these zones. Two types of solids are considered: pure condensates (Case 1) and a mixture of pure condensates and clathrates (Case 2). The model, calibrated to observed carbon enrichments, predicts deep compositions. In Case 1, argon is deeply depleted, while nitrogen, oxygen, krypton, phosphorus, sulfur, and xenon are significantly enriched relative to their protosolar abundances in the two planets. Case 2 predicts significant enrichments for all species, including argon, relative to their protosolar abundances. Consequently, Case 1 predicts near-zero Ar/Kr or Ar/Xe ratios, while Case 2 suggests that these ratios are 0.1 and 0.5–1 times their protosolar ratios, respectively. Both cases predict a bulk sulfur-to-nitrogen ratio consistent with atmospheric measurements.

Unified Astronomy Thesaurus concepts: Uranus (1751); Neptune (1096); Protoplanetary disks (1300); Exoplanet formation (492); Solid matter physics (2090); Planetary atmospheres (1244)

1. Introduction

Uranus and Neptune form a distinct and largely unexplored category of planets within our solar system. In recent years, these two ice giants have received increased attention from the scientific community, primarily due to the prevalence of exoplanets with similar masses and sizes, accounting for over half of the more than 5500 exoplanets discovered to date (Deleuil et al. 2020). Despite their importance, the vast distances to Uranus and Neptune have posed formidable challenges to their comprehensive study, with only limited data collected during the Voyager 2 flybys in 1986 and 1989 (Smith et al. 1986, 1989; Tyler et al. 1986; Lindal et al. 1987; Stone & Miner 1989; Lindal 1992). Consequently, our understanding of these distant worlds relies heavily on remote sensing techniques employed by Earth-based observatories and space telescopes (Karkoschka & Tomasko 2009; Fletcher et al. 2010, 2014; Karkoschka & Tomasko 2011; Feuchtgruber et al. 2013; Teanby & Irwin 2013; Cavalié et al. 2014; Orton et al. 2014a, 2014b; Sromovsky et al. 2014; Lellouch et al. 2015; Moreno et al. 2017; Irwin et al. 2018, 2019, 2021; Sromovsky et al. 2019; Teanby et al. 2021, 2022). Unfortunately, despite these advances, remote observations are not sufficient to provide direct, unambiguous measurements of the vertical atmospheric structure, composition, and cloud properties of Uranus and Neptune.

The US Decadal Survey has recommended the Uranus Orbiter and Probe (UOP) as the highest-priority flagship mission for the next decade.[8] This mission would send an orbiter to study Uranus's internal structure, along with an atmospheric entry probe to directly investigate the planet's atmosphere. By exploring an ice giant planet like Uranus, this mission aims to provide key insights into the formation and evolution of our solar system.

The present study is placed in the context of the preparation for the UOP mission and aims at providing predictions on the bulk volatile compositions of both Uranus and Neptune. A protoplanetary disk model is used, and the evolution of trace species is driven by the transport of the various vapors and solids present in the form of dust and pebbles (Schneeberger et al. 2023). Due to the high carbon abundance found in their envelopes (Irwin et al. 2019; Sromovsky et al. 2019), it is postulated that the two planets formed at the CO ice line within the protosolar nebula (PSN). This formation location matches their heavy-element compositions, as predicted by interior models, with the observed atmospheric D/H ratios (Feuchtgruber et al. 2013; Ali-Dib et al. 2014). The time evolution of the abundances of the major volatile species at the location of

[8] https://nap.nationalacademies.org/resource/26522/interactive/

the CO ice line is then calculated to derive the abundance ratios of the corresponding key elements, including the heavy noble gases, in the feeding zones of Uranus and Neptune. The supersolar metallicity of the envelopes of the two ice giants is thought to result from the accretion of solids formed in their feeding zones (Lambrechts et al. 2014; Helled & Fortney 2020). Two types of solids formed in the PSN are considered: solids composed of pure condensates and solids composed of a mixture of pure condensates and clathrates. The ratio between the two is determined at each time step and radius of the PSN as a function of the availability of volatiles in vapor form and crystalline water, as well as the equilibrium pressures of the different pure condensates and clathrates. Predictions for the deep compositions of Uranus and Neptune can then be made, assuming no significant compositional gradient in the interiors.

Section 2 provides an overview of the volatile transport and disk evolution model used in this study. In Section 3 we outline why the formation of ice giants near the CO ice line is a credible scenario. In addition, we provide a comprehensive overview of the assumptions underlying our composition model for the envelopes of Uranus and Neptune. In Section 4, we present the results of our simulations, outlining the compositions of solids and vapors, along with projections for elemental abundances deep within Uranus and Neptune. Finally, Section 5 is devoted to discussion and conclusions.

2. Volatile Transport and Disk Evolution Model

The disk and transport model utilized in this study is derived from the framework established by Schneeberger et al. (2023). Essentially, this model comprehensively describes the movement of dust particles and vapors within a time-dependent protoplanetary disk, drawing on methodologies outlined in Aguichine et al. (2020) and Mousis et al. (2020). This study explores two different scenarios: Case 1 corresponds to the scenario where solids can only crystallize as pure condensates, and Case 2 corresponds to the scenario where solids can crystallize as pure condensates and clathrates (see Figure 1 for an overview of the assumptions). The presence of amorphous ice is ruled out under the assumption that volatiles are exclusively delivered as vapors and pure condensates in the PSN. Elements of our model are explicitly described below.

2.1. Protoplanetary Disk Model

The evolution of the PSN's surface density is governed by the classical differential equation (Lynden-Bell & Pringle 1974):

$$\frac{\partial \Sigma_g}{\partial t} = \frac{3}{r}\frac{\partial}{\partial r}\left[r^{1/2}\frac{\partial}{\partial r}(r^{1/2}\Sigma_g \nu)\right], \tag{1}$$

which describes the time evolution of a viscous accretion disk of surface density, Σ_g, and dynamical viscosity, ν, assuming hydrostatic equilibrium in the azimuthal direction and invariance in the orbital direction. This equation can be reformulated into a pair of first-order differential equations that couple the gas surface density Σ_g field and the mass accretion rate $\dot{M}$:

$$\begin{cases} \dfrac{\partial \Sigma_g}{\partial t} = \dfrac{1}{2\pi r}\dfrac{\partial \dot{M}}{\partial r} \\ \dot{M} = 3\pi \Sigma_g \nu \left(1 + 2\dfrac{\partial \ln \nu \Sigma_g}{\partial \ln r}\right) \end{cases}. \tag{2}$$

The first equation embodies a mass conservation law, while the subsequent one represents a diffusion equation. The mass accretion rate is delineated as a function of the gas velocity field v_g by the expression $\dot{M} = -2\pi r \Sigma_g v_g$.

The viscosity coefficient ν is computed according to the prescription outlined in Shakura & Sunyaev (1973):

$$\nu = \alpha \frac{c_s^2}{\Omega_K}, \tag{3}$$

where α is the viscosity coefficient, c_s is the sound speed in the PSN, and Ω_K is the Keplerian frequency. The sound speed c_s is expressed as follows:

$$c_s = \sqrt{\frac{RT}{\mu_g}}, \tag{4}$$

where μ_g denotes the mean molecular mass of the gas in the PSN, which is taken here as 2.31 g mol^{-1}; T represents the midplane temperature; and R stands for the ideal gas constant.

Only viscous heating and the constant irradiation by the local environment of ambient temperature, T_{amb}= 10 K, are taken into account in our PSN model. Irradiation from the young Sun is neglected because the presence of shadowing is assumed in the outer part of the disk (Ohno & Ueda 2021). By doing so, the disk temperature is able to decrease down to the condensation temperature of Ar (~20 K) in the outer-planet region. Such a low disk temperature reached in the outer disk is supported by the in situ detection of Ar in comet 67P/Churyumov-Gerasimenko (hereafter 67P/C-G) by the Rosetta spacecraft (Balsiger et al. 2015). The temperature profile is determined by summing the production rates from both energy sources, as described by Hueso & Guillot (2005):

$$T^4 = \frac{1}{2\sigma_{SB}}\left(\frac{3}{8}\tau_R + \frac{1}{2\tau_P}\right)\Sigma_g \nu \Omega_K^2 + T_{amb}^4, \tag{5}$$

where σ_{SB} represents the Stefan–Boltzmann constant and τ_R and τ_P denote the Rosseland and Planck optical depths, respectively. In this context, we assume $\tau_P = 2.4\tau_R$, which corresponds to the opacity attributed to dust grains (Nakamoto & Nakagawa 1994). τ_R is determined from the Rosseland mean opacity κ_R using the following relation (Hueso & Guillot 2005):

$$\tau_R = \frac{\Sigma_g \kappa_R}{2}. \tag{6}$$

κ_R is calculated using a series of power laws expressed as $\kappa_R = \kappa_0 \rho^a T^b$, where ρ represents the gas density at the midplane and κ_0, a, and b are constants determined through fitting to observational data across various opacity regimes (Bell & Lin 1994).

The initial state of the model is computed based on the self-similar solution derived by Lynden-Bell & Pringle (1974):

$$\Sigma_g \nu \propto \exp\left[-\left(\frac{r}{r_c}\right)^{2-p}\right]. \tag{7}$$

Combining Equations (7) and (2) and assuming $p = \frac{3}{2}$, corresponding to the case of an early disk (Lynden-Bell & Pringle 1974), yields the initial profiles for the dust surface

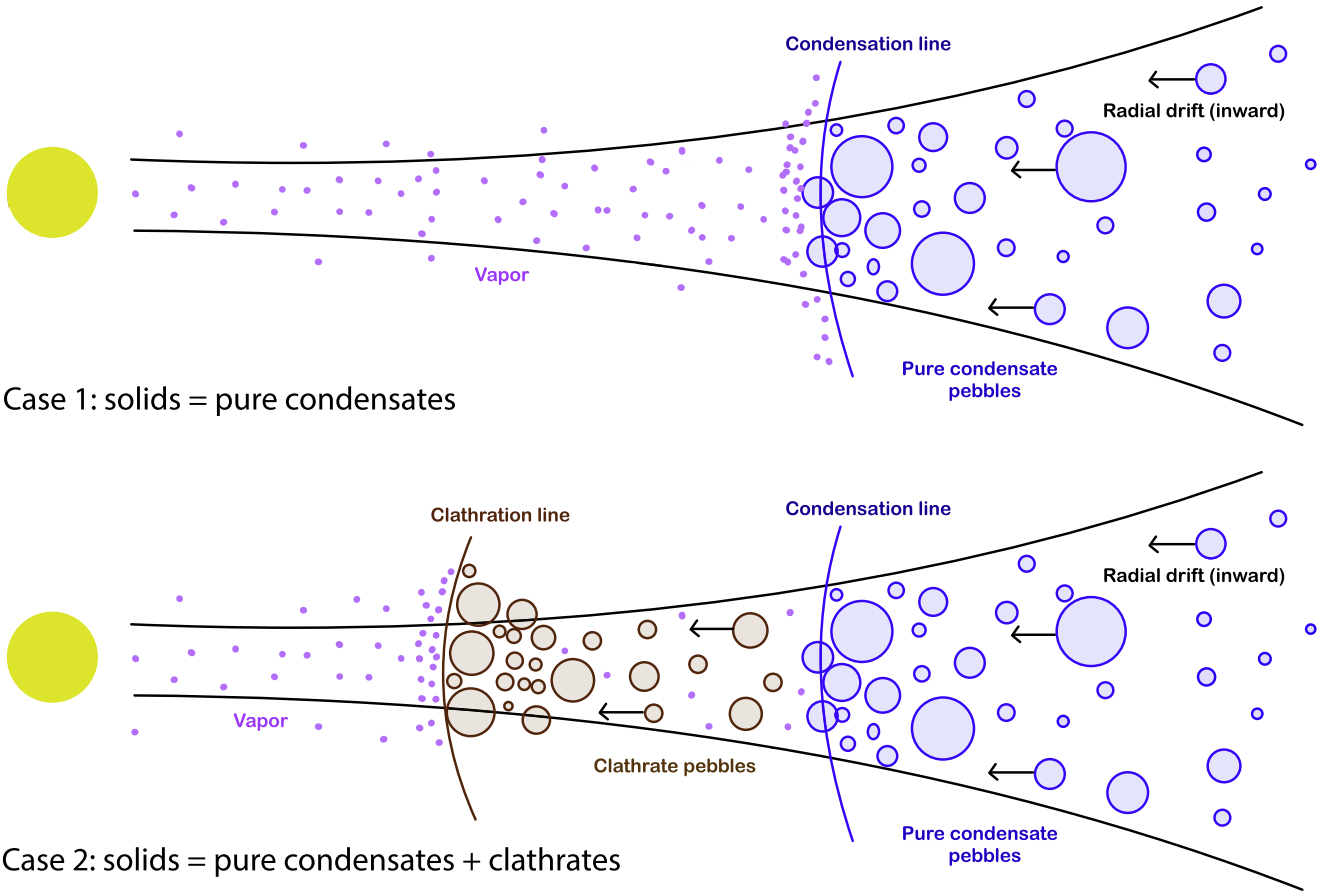

Figure 1. Phase changes of volatiles during their transport throughout the PSN. Volatiles are initially delivered as pure condensates in the PSN. Case 1 and Case 2 correspond to the scenarios where solids can only crystallize as pure condensates and can crystallize as pure condensates and clathrates, respectively. Pure condensate and clathrate pebbles are represented in blue and brown colors for a single species, respectively. Vapor is represented as purple circles. The condensation and clathration lines are represented as blue and brown solid lines, respectively. Once delivered to the disk, the phase of a given species is determined by the relative positions of the corresponding condensation, hydration, or clathration lines. Except for CO_2, which vaporizes at a higher temperature than its associated clathrate, hydration, or clathration lines of the considered volatiles are closer to the Sun than their respective ice lines. Gaseous volatiles condense or become entrapped (depending on the availability of water ice) when diffusing outward of the locations of their condensation, hydration, or clathration lines. Conversely, volatiles condensed or entrapped in grains or pebbles are released in vapor form when drifting inward of their lines.

density and mass accretion rate:

$$\begin{cases} \Sigma_{\rm g,0} = \dfrac{\dot{M}_{\rm acc,0}}{3\pi\nu}\exp\left[-\left(\dfrac{r}{r_c}\right)^{0.5}\right] \\ \dot{M}_0 = \dot{M}_{\rm acc,0}\left(1-\left(\dfrac{r}{r_c}\right)^{0.5}\right)\exp\left[-\left(\dfrac{r}{r_c}\right)^{0.5}\right] \end{cases}, \quad (8)$$

where r_c denotes the centrifugal radius and $\dot{M}_{\rm acc,0}$ represents the initial mass accretion rate onto the central star, set to $10^{-7.6}\,M_\odot\,{\rm yr}^{-1}$ (Hartmann et al. 1998). The total disk mass is assumed to be $0.1\,M_\odot$, with the majority (99%) of it confined within $\sim$200 au. Figure 2 represents the thermodynamic profiles of our nominal PSN model assuming $\alpha = 10^{-3}$ as in Schneeberger et al. (2023) and at $t = 10^4$, 10^5, and 10^6 yr of the disk evolution.

2.2. Dust Dynamics

The dust dynamics in our model follows the two-population algorithm developed by Birnstiel et al. (2012), which relies on the key idea that the dynamics of dust pebbles of many different sizes can be well approximated by the dynamics of only two populations of particles with different sizes (pebble and dust). The first group corresponds to a population of small grains with constant size of 0.1 μm. The second group represents a population of particles of pebble size (a few centimeters), which depends on the characteristics of the flow.

Within the disk, pebbles undergo growth through mutual sticking, governed by the following law:

$$a_1(t) = a_0\exp\left(\frac{t}{\tau_{\rm growth}}\right), \quad (9)$$

where $\tau_{\rm growth}$ represents the growth timescale, defined as

$$\tau_{\rm grow} = \frac{4\Sigma_g}{\sqrt{3}\,\epsilon_g\Sigma_b\Omega_{\rm K}}. \quad (10)$$

Σ_b denotes the total solid surface density and ϵ_g signifies the dust growth efficiency through mutual sticking, set to 0.5 (Lambrechts & Johansen 2014). Subsequently, we calculate the Stokes number of the pebbles as a function of their sizes,

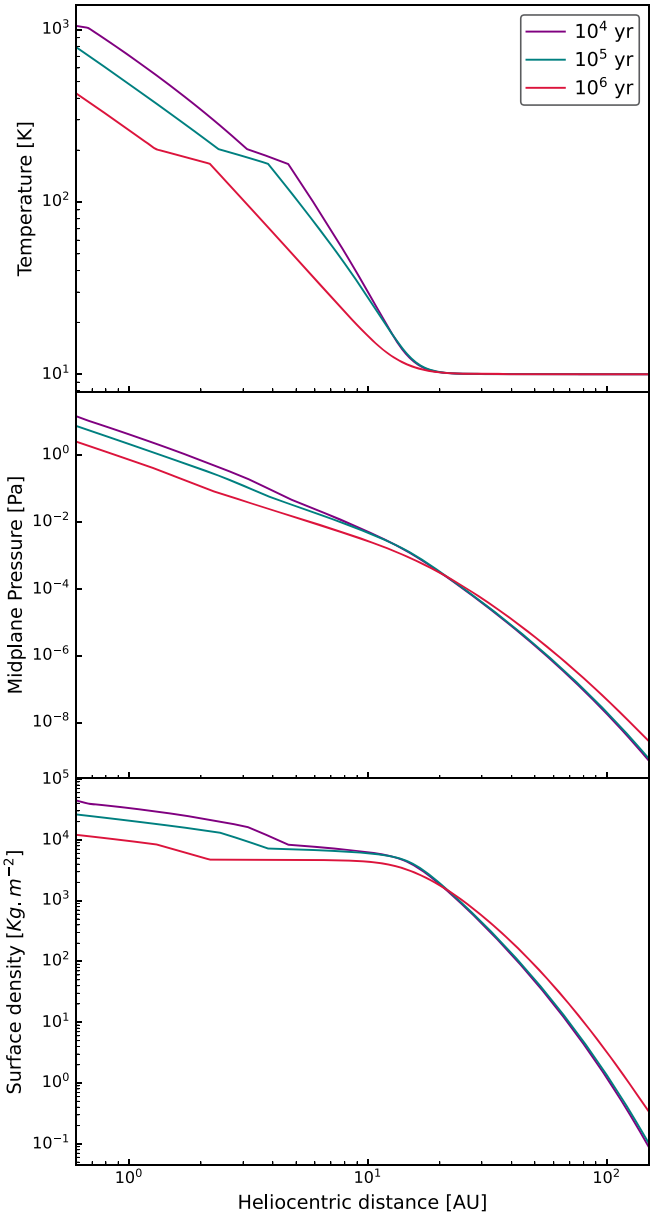

Figure 2. From top to bottom: profiles of the disk midplane temperature, pressure, and surface density calculated at $t = 10^4$, 10^5, and 10^6 yr as a function of heliocentric distance, assuming $\alpha = 10^{-3}$.

following the methodology outlined in Johansen et al. (2014):

$$\mathrm{St} = \begin{cases} \sqrt{2\pi}\dfrac{a_1 \rho_b}{\Sigma_g} \text{ if } a_1 \leqslant \dfrac{9}{4}\lambda \\ \dfrac{8}{9}\dfrac{a_1^2 \rho_b c_s}{\Sigma_g \nu} \quad \text{if} \quad a_1 \geqslant \dfrac{9}{4}\lambda \end{cases}. \tag{11}$$

The first and second cases correspond to the Epstein and Stokes regimes, respectively. The boundary between these regimes is determined by the gas mean free path $\lambda = \sqrt{\pi/2} \cdot \nu/c_s$, calculated by equating the terms in Equation (11). Here ρ_b represents the mean bulk density of the pebbles:

$$\rho_b = \frac{\sum_i \Sigma_{b,i} \rho_{b,i}}{\sum_i \Sigma_{b,i}}, \tag{12}$$

computed as the average of each species' bulk density $\rho_{b,i}$, weighted by their respective solid surface density $\Sigma_{b,i}$. In the following, we assume that all pebbles and grains have a density of 1 g cm^{-2} in the PSN, regardless of their compositions.

Observations suggest that disks are abundant in small dust particles, with fragmentation being a dominant process (Williams & Cieza 2011). Building on this observation, our approach incorporates fragmentation and radial drift as the primary growth-limiting mechanisms. These mechanisms impose an upper limit on the highest Stokes number attainable by particles. The first constraint arises from fragmentation, occurring when the relative speed between two pebbles due to turbulent motion exceeds a velocity threshold u_f. This upper limit, described by Birnstiel et al. (2012), is

$$\mathrm{St}_{\mathrm{frag}} = f_f \frac{1}{3\alpha}\frac{u_f^2}{c_s^2}, \tag{13}$$

where u_f and f_f are set to 10 m s^{-1} and 0.37, respectively.

Another constraint on dust growth arises from the drift velocities of various pebbles. When pebbles drift faster than they grow, it imposes an additional upper limit on the Stokes number (Birnstiel et al. 2012):

$$\mathrm{St}_{\mathrm{drift}} = f_d \frac{\Sigma_b v_{\mathrm{K}}^2}{\Sigma_g c_s^2} \left| \frac{d \ln P}{d \ln r} \right|^{-1}, \tag{14}$$

where P represents the disk midplane pressure, v_{K} denotes the Keplerian velocity, and f_d is set to 0.55.

When dust grains drift at high velocities and collide with other particles in their path, they may undergo fragmentation. This introduces a third upper limit for the Stokes number (Birnstiel et al. 2012), expressed as

$$\mathrm{St}_{\mathrm{df}} = \frac{1}{1-N}\frac{u_f v_{\mathrm{K}}}{c_s}\left(\frac{dP}{dr}\right)^{-1}, \tag{15}$$

where the factor $N = 0.5$ accounts for the observation that only larger grains tend to fragment upon collision.

In the algorithm, all limiting Stokes numbers are computed and compared with the Stokes number derived from Equation (11). At each time step, the smallest Stokes number found in this comparison becomes the reference Stokes number, which, in turn, sets a new value for the representative size a_1 for the large population. The representative size of the small population is always a_0, and their Stokes number is always computed in the Epstein regime.

Among the three size-limiting mechanisms, if particle drift is the most limiting one ($\mathrm{St}_{\mathrm{drift}} = \min(\mathrm{St}_{\mathrm{frag}}, \mathrm{St}_{\mathrm{drift}}, \mathrm{St}_{\mathrm{df}})$), then the fraction of the mass contained in the large population is $f_m = 0.97$. Otherwise, f_m is set to 0.75 (Birnstiel et al. 2012). The mean grain size $\bar{a}$ is then given by

$$\bar{a} = f_m a_1 + (1 - f_m)\, a_0. \tag{16}$$

2.3. Trace Species Evolution Model

Trace species are accounted for in three distinct forms within our model: vapors, pure condensates, and those entrapped in clathrate. Each of these forms is assigned a distinct surface density denoted by $\Sigma_{v,i}$, $\Sigma_{p,i}$, and $\Sigma_{c,i}$ for species i in the vapor, pure condensate, and clathrate/hydrate phases, respectively. Their temporal and radial evolution is governed by the

advection–diffusion equation (Birnstiel et al. 2012; Desch et al. 2017):

$$\frac{\partial \Sigma_i}{\partial t} + \frac{1}{r}\frac{\partial}{\partial r}\left[r\left(\Sigma_i v_i - D_i \Sigma_g \frac{\partial}{\partial r}\left(\frac{\Sigma_i}{\Sigma_g}\right)\right)\right] - \dot{Q}_i = 0, \quad (17)$$

where D_i denotes the diffusion coefficient, v_i represents the radial speed, and $\dot{Q}_i$ is a source/sink term that accommodates phase changes, with positive/negative values indicating creation/loss of matter.

Regarding vapor surface densities, we assume $D_i = D_g$ and $v_i = v_g$, as vapors are closely coupled to the PSN gas and evolve similarly. Following Shakura & Sunyaev (1973), the gas diffusivity D_g equals the viscosity ν, and the gas velocity is

$$v_g = -\frac{\dot{M}_{\rm acc}}{2\pi r \Sigma_g}. \quad (18)$$

At each time and location, we assume that dust particles form from a mixture of all available solids. Consequently, species trapped in hydrates and amorphous ice possess the same diffusion coefficient D_s and radial velocity v_s as the pure condensates. Following the approach of Birnstiel et al. (2012), the diffusion coefficient of solids is determined by

$$D_s = \frac{D_g}{1 + {\rm St}^2}. \quad (19)$$

The dust radial velocity is represented as the sum of gas drag and drift velocities, as described by Birnstiel et al. (2012):

$$v_s = \frac{1}{1 + {\rm St}^2} v_g + \frac{2{\rm St}}{1 + {\rm St}^2} v_{\rm drift}, \quad (20)$$

where the drift velocity is given by Weidenschilling (1997):

$$v_{\rm drift} = \frac{c_s^2}{v_{\rm K}} \frac{d \ln P}{d \ln r}. \quad (21)$$

The diffusion coefficient and radial velocity of solids are computed separately for the small and large populations, corresponding to particles of sizes a_0 and a_1, respectively. Subsequently, the diffusion coefficient D_s and radial velocity v_s employed to evolve surface densities of solids are determined as mass-averaged diffusivities and velocities of the small and large populations, as outlined by Birnstiel et al. (2012):

$$\begin{cases} v_s = f_m v_{d,a_0} + (1 - f_m) v_{d,a_1}. \\ D_s = f_m D_{d,a_0} + (1 - f_m) D_{d,a_1}. \end{cases} \quad (22)$$

2.4. Sources and Sinks of Trace Species

We adopt the methodology outlined in Aguichine et al. (2020) for illustrating the sources and sinks for both solid and vapor phases of the different species. If the partial pressure of a species i's pure condensate falls below its equilibrium pressure $P_{{\rm eq},i}$, it undergoes sublimation. This sublimation process introduces a sink term for pure condensates within each time step Δt, as detailed in Drażkowska & Alibert (2017):

$$\dot{Q}_{p,i} = -\min\left(\sqrt{\frac{8\pi\mu_i}{RT}} \frac{3}{\pi \bar{a} \bar{\rho}} P_{{\rm eq},i} \Sigma_{p,i}; \frac{\Sigma_{p,i}}{\Delta t} \right). \quad (23)$$

Here μ_i represents the molar mass of species i, $\bar{\rho}$ stands for the mean bulk density of grains, $P_{{\rm eq},i}$ denotes the equilibrium pressure, and $\bar{a}$ signifies the mean size of the grains. The latter part of this condition ensures that the quantity of pure condensate sublimated does not exceed the available amount. Details concerning the equilibrium curves of pure condensates can be found in the work of Schneeberger et al. (2023).

Conversely, gas of species i transitions into a pure condensate when its partial pressure surpasses the corresponding equilibrium pressure. This condensation process contributes to source terms for pure condensates, as elaborated in Drażkowska & Alibert (2017):

$$\dot{Q}_{p,i} = \min\left((P_i - P_{{\rm eq},i}) \frac{2H\mu_i}{RT\Delta t}, \frac{\Sigma_{v,i}}{\Delta t} \right). \quad (24)$$

We have incorporated the possibility of clathrate crystallization in the PSN. Assuming an ample supply of crystalline water, these solids are the first to form during the disk cooling phase, due to their higher crystallization temperatures compared to those of corresponding pure condensates. The sole exception to this trend is CO_2, which condenses at a higher temperature than its clathrate under nebular conditions. This implies that CO_2 pure condensate is considered as the only solid form of CO_2 in this model. Furthermore, our model operates under the assumption that NH_3 solely exists in its pure condensate form at $t = 0$ in the PSN. Consequently, NH_3 monohydrate cannot form, as its equilibrium curve lies at a lower temperature in the disk compared to its pure condensate. The computation of source/sink terms follows the same methodology as for pure condensates (Equations (23) and (24)), utilizing equilibrium pressures specific to clathrate hydrates instead of those for pure condensates. Detailed equilibrium curves for various clathrates can be found in the work of Schneeberger et al. (2023). Moreover, the formation of clathrates necessitates an adequate presence of crystalline water for trapping. This imposes a constraint on the hydrate source term $\dot{Q}_{c,i}$:

$$\dot{Q}_{c,i}\, \Delta t \leqslant \frac{\mu_i}{S_i\, \mu_{\rm H_2O}} \left[\Sigma_{p,{\rm H_2O}} - \sum_k \Sigma_{c,k} \frac{S_k\, \mu_{\rm H_2O}}{\mu_k} \right]. \quad (25)$$

Here μ_i represents the molar mass of species i, $\mu_{\rm H_2O}$ denotes the molar mass of crystalline water, and S_k signifies the stoichiometric ratio between species k and water. This ratio is specifically set to 5.75 and 5.66 for type I and type II clathrates, respectively.

This expression compares the available amount of crystalline water $\Sigma_{p,{\rm water}}$ with the quantity needed to form all clathrates. Throughout the evolution of the disk, this condition is evaluated at each time and location where thermodynamic conditions allow for clathrate formation. It is constructed by assessing the amount of crystalline water available for clathration (as indicated within brackets). If water availability is not a limiting factor, the condition is satisfied. However, if solid water is insufficient, a new hydrate source term ($\dot{Q}_c$) is derived from Equation (25).

In all scenarios, a prioritization mechanism is employed based on the disparity between P_i and $P_{{\rm eq},i}$. When conditions conducive to clathrate formation are met, the term $P_i - P_{\rm eq,i}$ yields a positive value. Priority for trapping is accorded to the species with the highest difference value.

From the combined rates of condensation and crystallization, the overall sink and source term for vapor can be derived as

Table 1
Initial Gas-phase Abundances of the Considered Species

Trace Species	$(X/H_2)_\odot$	Trace Species	$(X/H_2)_\odot$
H_2O	8.86×10^{-4}	NH_3	5.81×10^{-5}
CO	2.42×10^{-4}	PH_3	6.62×10^{-7}
CO_2	9.68×10^{-5}	Ar	7.78×10^{-6}
CH_4	2.42×10^{-5}	Kr	4.08×10^{-9}
H_2S	1.74×10^{-5}	Xe	4.38×10^{-10}
N_2	5.81×10^{-5}	…	…

follows:

$$\dot{Q}_{v,\,i} = -\dot{Q}_{p,\,i} - \dot{Q}_{c,\,i}. \tag{26}$$

The initial PSN gas-phase composition is given in Table 1. The mixing ratios are identical to those adopted by Schneeberger et al. (2023) in the PSN, but the protosolar elemental abundances have been updated by using the data from Lodders (2021). We assume that half of C is sequestrated in refractory matter (Bergin et al. 2015). The other half of C is distributed between CO, CO_2, or CH_4, and the remaining O forms H_2O. $CO{:}CO_2{:}CH_4$ and $N_2{:}NH_3$ molecular ratios are assumed to be 10:4:1 and 1:1 in the PSN gas phase, respectively. The $CO{:}CO_2$ and $CO{:}CH_4$ ratios are derived from Rosetta measurements of comet 67P/C-G (Mousis et al. 2014; Le Roy et al. 2015). $N_2{:}NH_3$ is assumed to be 1:1, a value predicted by thermochemical models taking into account catalytic effects of Fe grains on the kinetics of N_2-to-NH_3 conversion in the PSN (Fegley 2000; Mousis et al. 2009). Sulfur is assumed to be half in H_2S form and half in refractory sulfide components (Pasek et al. 2005).

3. Ice Giant Formation at the Location of the CO Ice Line

With values reaching roughly 100 times the protosolar value (see Section 4), Uranus and Neptune exhibit the most pronounced carbon enrichments among the four giants in our solar system (Mousis et al. 2022). This implies that carbon was a major ingredient in the composition of the vapors and solids from which the two ice giants formed. The formation of Uranus and Neptune at the CO ice line has been previously proposed by Ali-Dib et al. (2014). This scenario is based on the presence of significant amounts of carbon-rich solids at the CO ice line location, allowing the reconciliation of the observed D/H ratio in the envelopes of Uranus and Neptune with the amount of heavy elements predicted by interior models. In this region of the PSN, CO abundance surpasses that of water, due to its higher surface density concentrated at its ice line position (Ali-Dib et al. 2014). The accretion process of volatile material by the two ice giants appears to favor carbon-rich ices over water ice. This discrepancy could shed light on why their measured D/H ratios ($\sim$(4.1–4.4) $\times 10^{-5}$) lie between the protosolar value observed in Jupiter ($\sim 2 \times 10^{-5}$) and the higher D-rich values observed in comets ($\sim$(1.5–6) $\times 10^{-4}$; Feuchtgruber et al. 2013). A scenario where a higher fraction of CO is accreted alongside a smaller fraction of cometary ice might align with the observed ratios (Ali-Dib et al. 2014). Past models struggled to reconcile the observed D/H ratio in Uranus and Neptune with building blocks exhibiting cometary values, primarily because they assumed primordial water as the primary form of accreted solids (Feuchtgruber et al. 2013).

Figure 3 depicts the radial profiles of the C/H ratio relative to its protosolar abundance (Lodders 2021) and calculated in

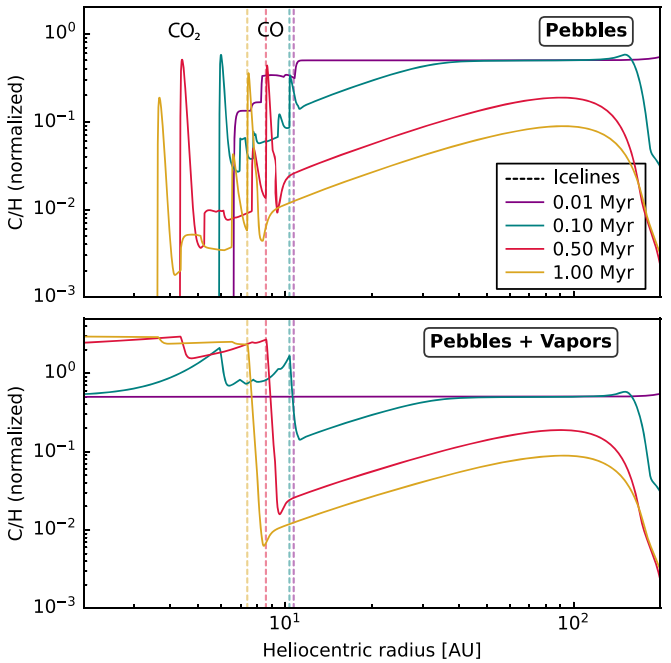

Figure 3. Radial profiles of the C/H ratio relative to its protosolar abundance, calculated as a function of time in the PSN and in Case 2, assuming $\alpha = 10^{-3}$. Top and bottom panels correspond to the C/H ratio calculated in pebbles and in pebbles + vapors, respectively. Vertical dashed lines indicate CO ice line locations across PSN evolution (each color corresponds to a different epoch).

Case 2. This analysis assumes that the solids formed consist primarily of pure condensates and clathrates within the PSN. These profiles are calculated over time in the PSN for both solids and a combination of solids and gas. At each epoch under consideration, the abundances of solids are zero in regions interior to their corresponding ice lines. In this study, we define the ice line of a specific species i as the boundary where the solid-phase surface density $\Sigma_{\mathrm{sol},i}$ equals the vapor-phase surface density $\Sigma_{\mathrm{vap},i}$. This boundary effectively separates the region dominated by ice i from the region dominated by vapor. Consequently, the position of the ice line is governed by both the partial pressure of species i and its corresponding equilibrium vapor pressure. In Figure 3, the C/H ratio exhibits two distinct enrichment peaks beyond a few thousand years of PSN evolution, located precisely at the CO_2 and CO pure condensate ice lines. These two peaks correspond to the outward diffusion of vapors across the ice line boundaries, where they undergo condensation and accumulate as solid grains at these specific locations. While CO is initially more abundant than CO_2 in the gas phase of the PSN, the slightly more pronounced enrichment peak of CO_2, positioned at a closer heliocentric distance, is attributed to pebbles drifting at higher velocities along their journey inward of the disk. This phenomenon leads to a more substantial accumulation of CO_2 in this region of the PSN. In this manner, the mass flux of pebbles crossing the CO_2 ice line increases, more than compensating for the lower abundance of CO_2. The subtle deviations between the two prominent peaks correspond to minor peaks arising from the condensation/vaporization sequences of CH_4 clathrate, CO clathrate, and CH_4 pure condensate, respectively, as distance from the Sun increases. Plots based on Case 1 would be similar to those in Figure 3, but without these small variations.

The C/H enrichment profiles highlight the ease of forming carbon-rich planets from both gases and solids at the CO_2 or CO ice lines. In the following, we presume that Uranus and Neptune originated from vapors, pebbles, and planetesimals located at the CO ice line. This hypothesis extends the scope for the formation of the four giants between the H_2O and CO ice lines. Specifically, it has been postulated that Jupiter's formation likely took place in proximity to the water ice line (Drażkowska & Alibert 2017). Moreover, alternative theories suggest that Jupiter might have originated near the N_2 ice line, which could explain its supersolar enrichments in nitrogen and heavy noble gases as detected by the Galileo probe (Öberg & Wordsworth 2019; Bosman 2019). These alternative scenarios advocate for a delayed formation (potentially up to 1 Myr in our model—see Section 4) of Uranus and Neptune at the CO ice line. This delay would have been necessary, as the two ice giants would have needed to wait for Jupiter (and Saturn) to migrate inward before they could start forming themselves.

Our model centers on analyzing the composition of solids and vapors that form and/or evolve within the PSN to provide an estimate of the bulk compositions of the envelopes of Uranus and Neptune. Our primary assumption is that the composition of solids accreted by the two ice giants is fixed during the disk phase and does not evolve during their incorporation by the forming planets. Our sole conjecture concerning planetary formation is that the two ice giants have mostly grown from solids, and gases to a lower extent, situated at the CO ice line because it is the most favorable location to form C-rich material, in agreement with the high carbon enrichment observed in the envelopes (see Section 4). Our determination is based on the principle that the heavy elements found in the planetary envelopes were largely supplied by solids during the accretion phase and/or, eventually, by subsequent core erosion (Lambrechts et al. 2014; Helled & Fortney 2020). The composition of these solids mirrors that of the grains that crystallized within the planets' feeding zones in the PSN.

One should note that, even if our model computes the evolution of the composition of dust and pebbles (with sizes in the micron-to-centimeter range) through the different ice lines of the PSN, it does not exclude the accretion of larger planetesimals by Uranus and Neptune. Since these solids agglomerated from smaller grains/particles via, for example, streaming instability in the PSN (Rucska & Wadsley 2023), their composition is fixed by those of their constituting particles and pebbles.

4. Results

This section is composed of two parts. The first part explores the composition of solids and vapors evolving around the CO ice line in the PSN. The second part focuses on forecasting the overall abundances within the envelopes of Uranus and Neptune.

4.1. Composition of Solids and Vapors at the CO Ice Line

Figure 4 represents the molar abundance profiles of H_2O, NH_3, CO_2, H_2S, Xe, CH_4, PH_3, Kr, CO, Ar, and N_2 in vapors and solids, at different epochs of PSN evolution. The figure illustrates a scenario where vapors exclusively transition into pure condensates during the cooling of the PSN (Case 1). At $t = 10$ kyr of disk evolution, the pure condensates start to vaporize as they drift inward in the form of grains, upon penetrating regions interior to approximately 11.2 au (N_2), 10.9 au (Ar), 10.7 au (CO), 10.2 au (Kr), 9.9 au (PH_3), 9.9 au (CH_4), 9.0 au (Xe), 7.0 au (H_2S), 6.6 au (CO_2), 6.2 au (NH_3), and 3.3 au (H_2O) from the Sun within the PSN. All grains are vaporized once they have drifted inward past the ice line of H_2O. At $t = 100$ kyr, the cooling of the PSN brings the sublimation region of the grains closer to the Sun, typically spanning from ∼2.6 to 11.0 au from the Sun. At $t = 1$ Myr, the icy grains sublimate at closer heliocentric distances, namely in the region 1.4–8.0 au from the Sun.

Figure 5 is analogous to Figure 4, but it includes the possibility that vapors transition into solids composed of either clathrates or pure condensates (Case 2). Here the positions of the ice lines of pure condensates align with those of Figure 4. Comparing the two figures shows that clathrates can persist several au closer to the Sun compared to their corresponding pure condensates. With the exception of H_2O, CO_2, and NH_3, which exist solely in their pure condensate forms, all other solid grains are completely vaporized upon crossing the clathrate lines. These lines are positioned closer to the Sun with respect to those of the pure condensate forms, at ∼8.4 au (N_2), 9.0 au (Ar), 8.2 au (CO), 8.5 au (Kr), 6.9 au (PH_3), 7.6 au (CH_4), 7.4 au (Xe), and 6.4 au (H_2S) from the Sun at 10 kyr of PSN evolution. The abundance of clathrates in the solid phase is contingent on the availability of crystalline water, which itself is influenced by the fraction of carbon present in oxidized C-bearing volatiles. With the assumed mixing ratios in the initial PSN gas phase (see Section 2.4), clathrates can be as abundant as the corresponding pure condensates at closer heliocentric distances, dominating the composition of solids formed in the vicinity of their ice lines.

Figures 6 and 7 depict the temporal evolution of the total elemental ratios (Ar/C, N/C, O/C, Kr/C, P/C, S/C, and Xe/C) relative to their protosolar values in Case 1 and Case 2, respectively. These ratios are calculated by summing the contributions from both solid and solid+vapor phases at the precise location of the CO ice line in the PSN. The CO ice line gradually migrates inward from approximately 10.7 au to about 7.2 au within the first megayear of the PSN evolution. P/C, S/C, and Xe/C elemental ratios appear superimposed in the two figures because all P, S, and Xe elements are locked into single species (H_2S, PH_3, and Xe) that form pure condensates evolving in a similar manner at the location of the CO ice line. At the beginning, all ratios are protosolar in the disk, which takes several dozen thousands of years of evolution to enable the transport of enough matter and form the different enrichment peaks.

In both Case 1 and Case 2, when considering the dual contribution of vapors+solids, the global Ar/C ratio rapidly evolves toward a plateau slightly higher (∼1.5 times) than its protosolar ratio because of the significant contribution of Ar vapor at the CO ice line location. Remarkably, even though only 0.7 times the protosolar ratio after 1 Myr of PSN evolution, the Ar/C ratio is orders of magnitude higher in solids in Case 2 compared to Case 1 (10^{-25} at the same epoch). This results from the presence of Ar clathrate at the CO ice line, while pure Ar still fails to condense at this location.

In both cases, the global N/C and O/C ratios decrease down to plateaus reaching ∼0.9–1 and 0.3 times their protosolar ratios, respectively. This decrease is primarily due to an increase in the amount of solid CO at its ice line. The N/C ratio

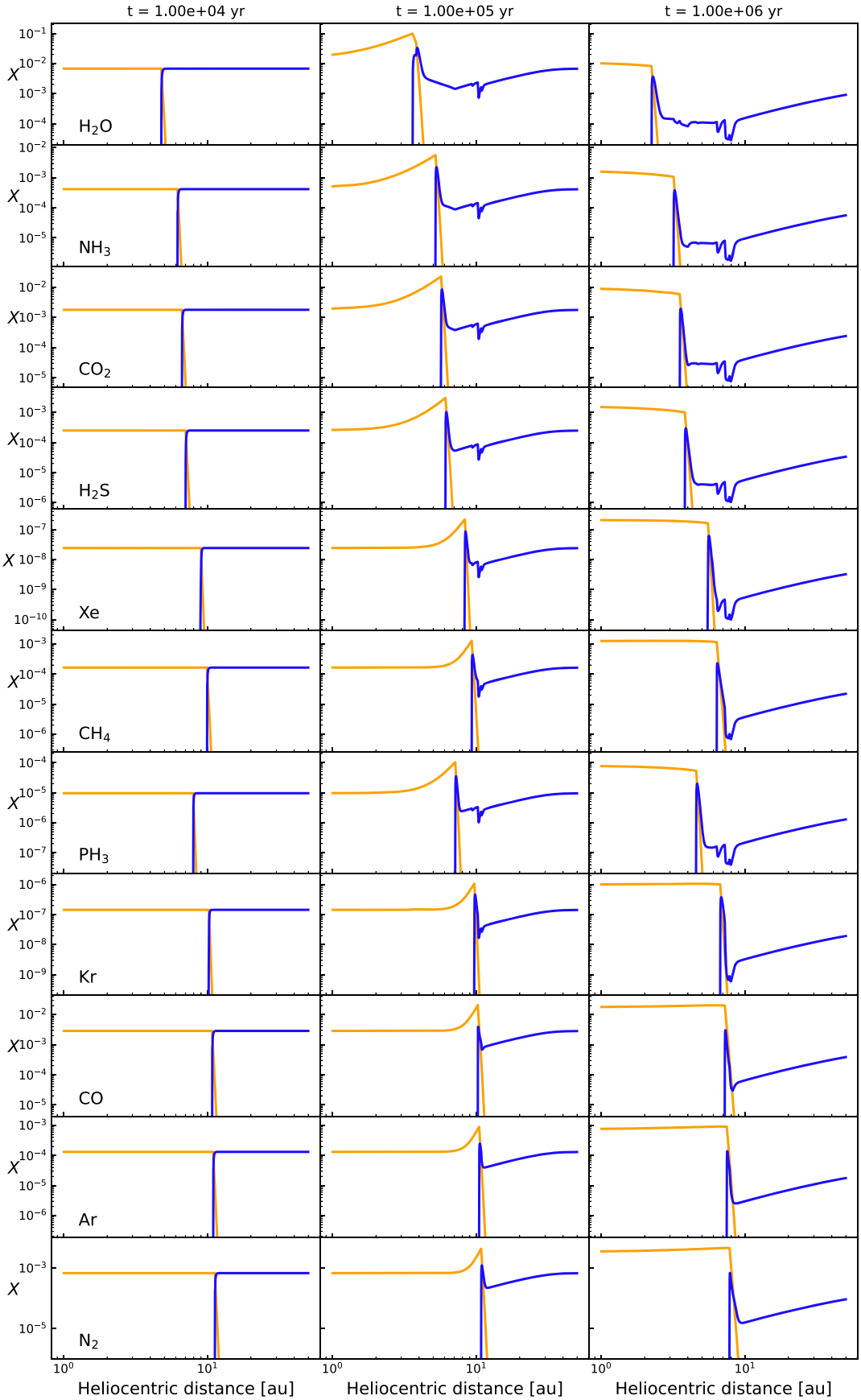

Figure 4. Molar abundance profiles of various volatile species in gaseous (orange lines) and pure condensate (blue lines) forms, calculated at different epochs (10^4, 10^5, and 10^6 yr) of the PSN evolution (Case 1). The species shown are H_2O, NH_3, CO_2, H_2S, Xe, CH_4, PH_3, Kr, CO, Ar, and N_2.

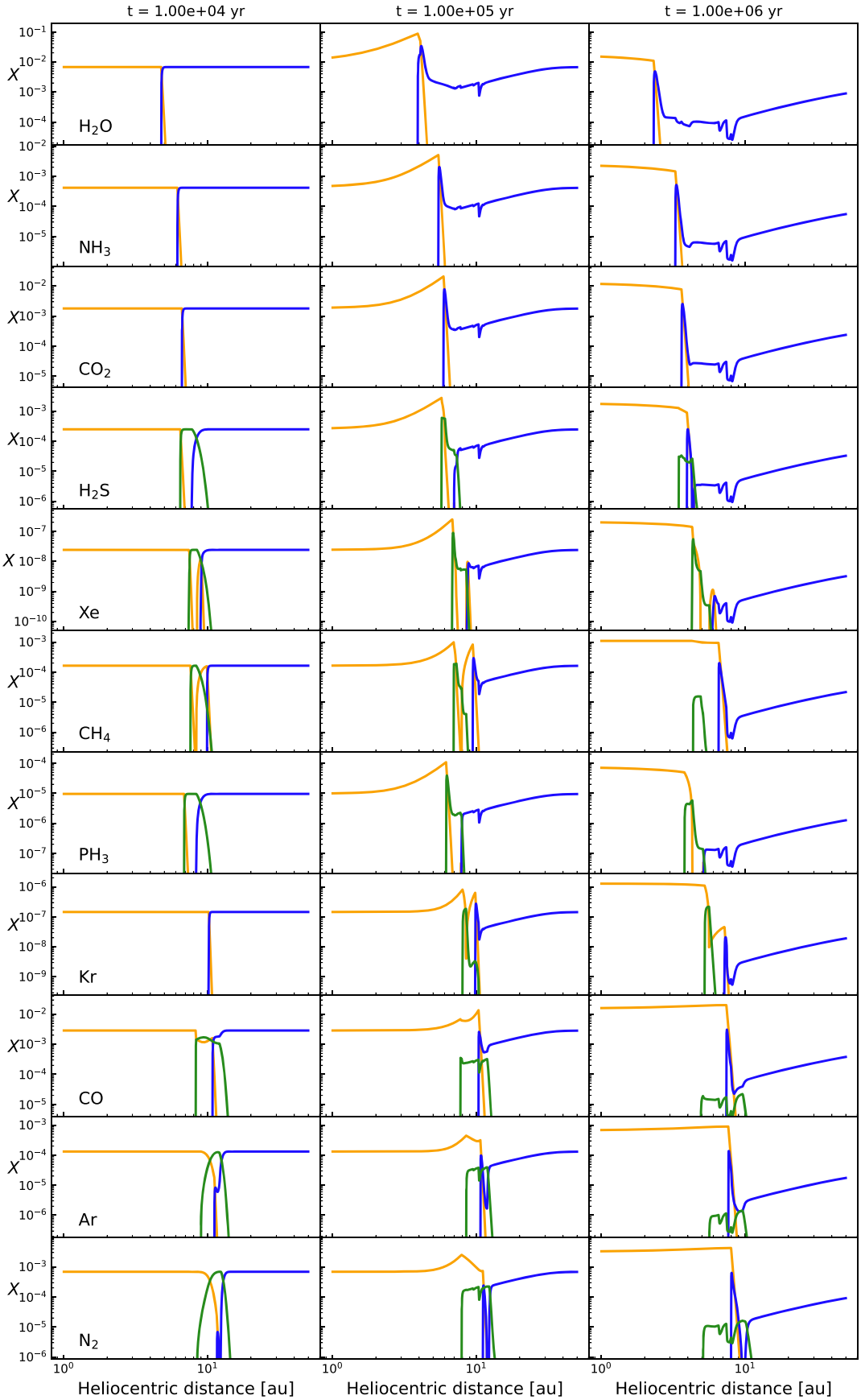

Figure 5. Molar abundance profiles of various volatile species in gaseous (orange lines), clathrate (green lines), and pure condensate (blue lines) forms, calculated at different epochs (10^4, 10^5, and 10^6 yr) of the PSN evolution (Case 2). The species shown are H_2O, NH_3, CO_2, H_2S, Xe, CH_4, PH_3, Kr, CO, Ar, and N_2.

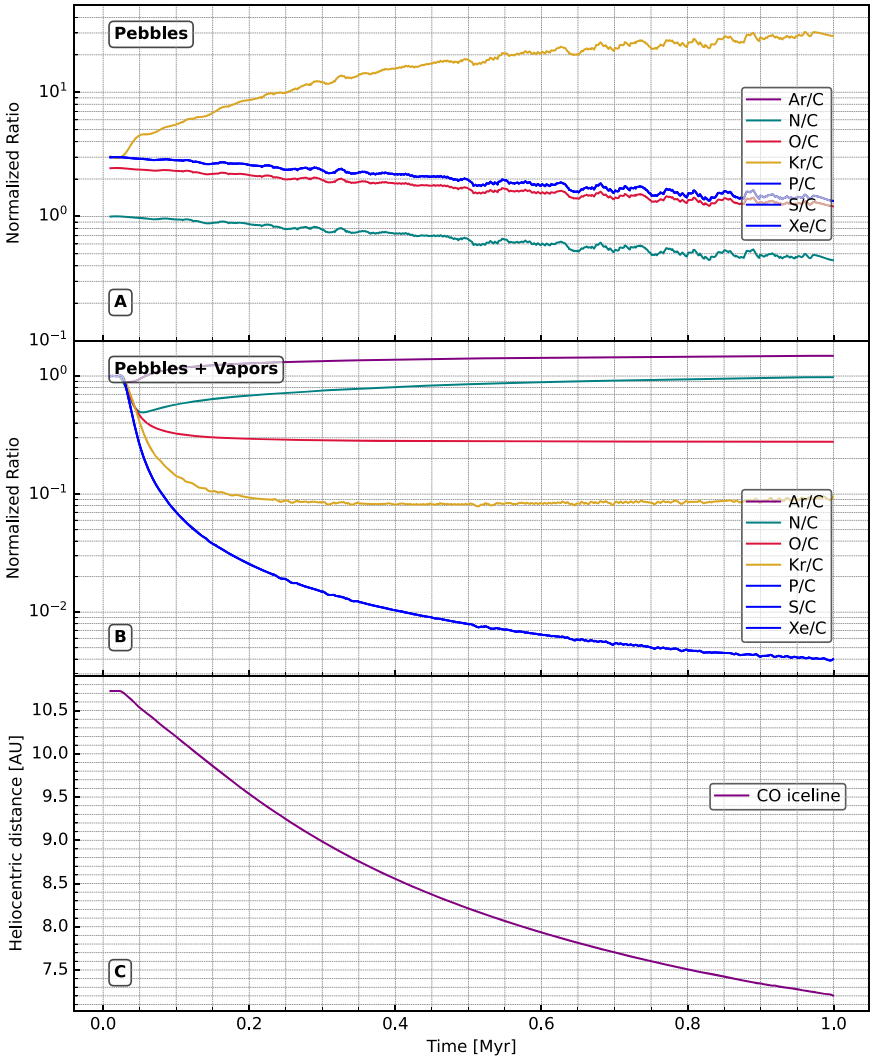

Figure 6. (a) Temporal evolution of elemental ratios (Ar/C, N/C, O/C, Kr/C, P/C, S/C, and Xe/C) calculated in Case 1 for solid condensates at the CO ice line within the PSN. The ratios are adjusted to their protosolar values. The P/C, S/C, and Xe/C ratios appear superimposed in the panel (see text for details). The Ar/C ratio is not represented in the solids because it falls below 10^{-25} (see text). (b) Same elemental ratios as in panel (a), but summed over both solid and vapor phases within the PSN. (c) Temporal evolution of the position of the CO ice line within the PSN.

in solids is three times higher in Case 2 compared to Case 1. This difference can be attributed to a significant portion of N_2 being sequestered in N_2 clathrate in Case 2, whereas solid N_2 is nearly absent at the CO ice line. Similarly, the decrease of the global Kr/C ratio is more pronounced in Case 2 ($\sim 0.04 \times (\mathrm{Kr/C})_\odot$) than in Case 1 ($\sim 0.1 \times (\mathrm{Kr/C})_\odot$) after 1 Myr of PSN evolution. This reduction is attributed to the presence of Kr clathrates closer to the Sun in Case 2. These Kr clathrates effectively sequester a significant amount of vapor, thereby reducing the portion that can diffuse outward from the disk.

In both Case 1 and Case 2, the increase in the CO surface density at the location of its ice line is the primary cause of the steep decreases in the global P/C, S/C, and Xe/C ratios to less than 4×10^{-3} their protosolar ratios after 1 Myr of PSN evolution. This is because the ice lines of PH_3, H_2S, and Xe are located at closer heliocentric distances than that of CO in the PSN. Consequently, these relative ratios become more sensitive to the sharp increase in the CO abundance.

4.2. Predicted Bulk Elemental Abundances

Figures 8 and 9 further illustrate the translation of the Ar/C, N/C, O/C, Kr/C, P/C, S/C, and Xe/C ratios into bulk elemental enrichments relative to the protosolar elemental abundances in the envelopes of Uranus and Neptune in Case 1 and Case 2, respectively. These elemental ratios are also computed as a function of the time evolution of the PSN. To calibrate the model, we use the observed carbon enrichments that have been measured remotely in Uranus and Neptune. Specifically, we multiply the Ar/C, N/C, O/C, Kr/C, P/C, S/C, and Xe/C ratios computed in solids by the measured carbon abundances in the atmospheres of Uranus and Neptune. This approach allows us to infer the overall enrichment levels of other key elements in the envelopes of these ice giant planets, based on their measured carbon enrichment. By tying the other elemental abundances to the measured carbon abundances, we can obtain an estimate of the bulk composition of the atmospheres of Uranus and Neptune. In each figure, the predicted bulk abundances in Uranus and Neptune correspond

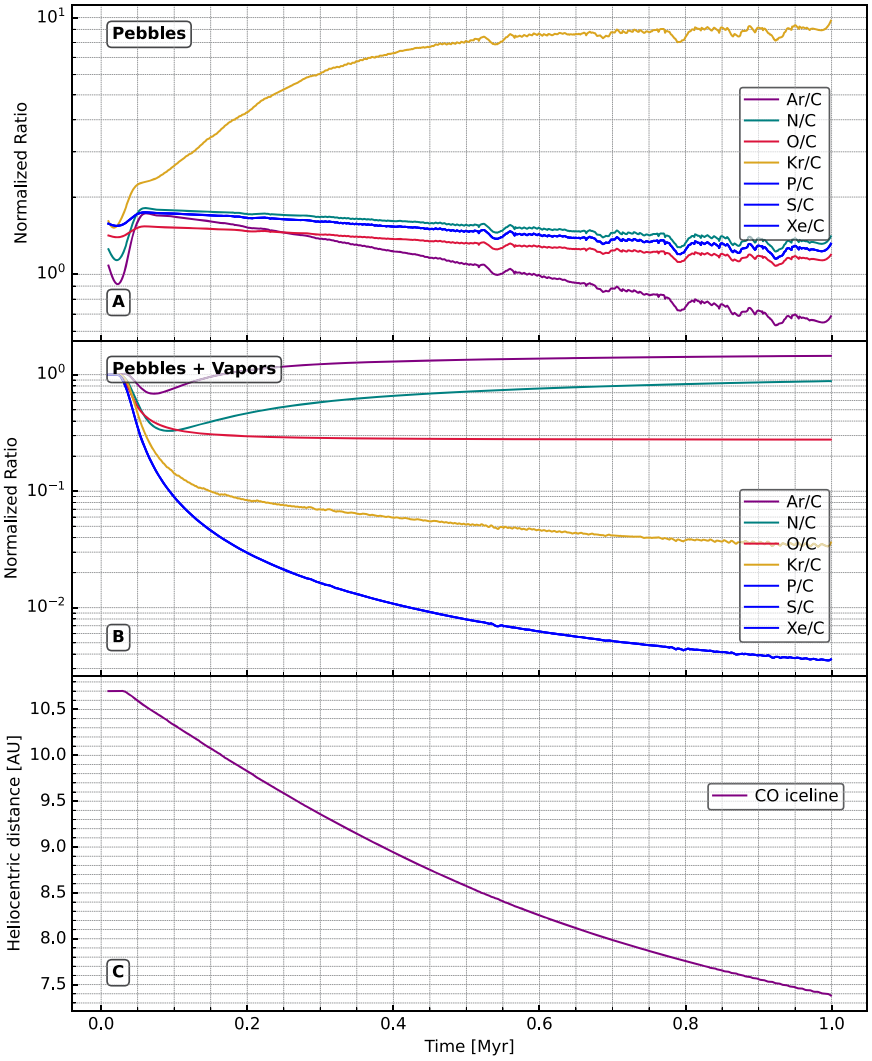

Figure 7. Same as Figure 6, but for Case 2.

to the scenario where the metallicities of the two planets' envelopes have been primarily supplied by the delivery of solid materials, either from the dilution of their cores or during the accretion process of the forming planets. Table 2 extracts the predictions for volatile enrichments in the envelopes of Uranus and Neptune from Figures 8 and 9, assuming that their heavy elements were acquired from the PSN at 0.5 and 1 Myr of its evolution. Most of the volatile abundance predictions reach steady-state conditions after 1 Myr of PSN evolution.

In the case of Uranus, a CH_4 abundance is set between 2.4% and 3% (Sromovsky et al. 2019), corresponding to an enrichment factor that is ∼40–50 times the protosolar value (Lodders 2021), and adopting the He abundance derived from Voyager 2 observations (Conrath et al. 1987). In the case of Neptune, the CH_4 abundance ranges between 4% and 6% (Irwin et al. 2019), leading to an enrichment factor that is ∼68–104 times the protosolar value (Lodders 2021), and adopting the He abundance derived from Infrared Space Observatory long-wavelength observations (Burgdorf et al. 2003).

Assuming that the heavy elements present in Uranus's envelope were supplied solely by solids formed in the PSN at 0.5 Myr (or 1 Myr) of evolution, the model predicts the following enrichment or impoverishment in volatiles in Case 1:

1. Ar is absent from the envelopes or severely depleted.
2. N, O, and Kr are enriched by factors of 26.2–32.8 (17.7–22.2), 67.2–84.0 (48.2–60.3), and 729.7–912.2 (1135.9–1419.8), respectively, with respect to their protosolar values.
3. P, S, and Xe are all enriched by a similar factor of 78.7–98.4 (53.2–66.6), with respect to their protosolar values.

The depletion of Ar arises from the fact that it condenses at a greater heliocentric distance compared to the CO ice line. Although the predicted volatile abundances from solids formed at 1 Myr of PSN evolution are slightly different from the 0.5 Myr case, they remain qualitatively similar. The key distinctions are the lower enrichment factors for N, O, P, S, and Xe at 1 Myr, while Kr exhibits a higher enrichment factor compared to the 0.5 Myr case.

Under the same assumptions regarding formation conditions, our remarks on volatile abundances are also valid for Neptune. Apart from the strong depletion of Ar, which is consistent with both cases, the higher enrichments of other volatiles correspond

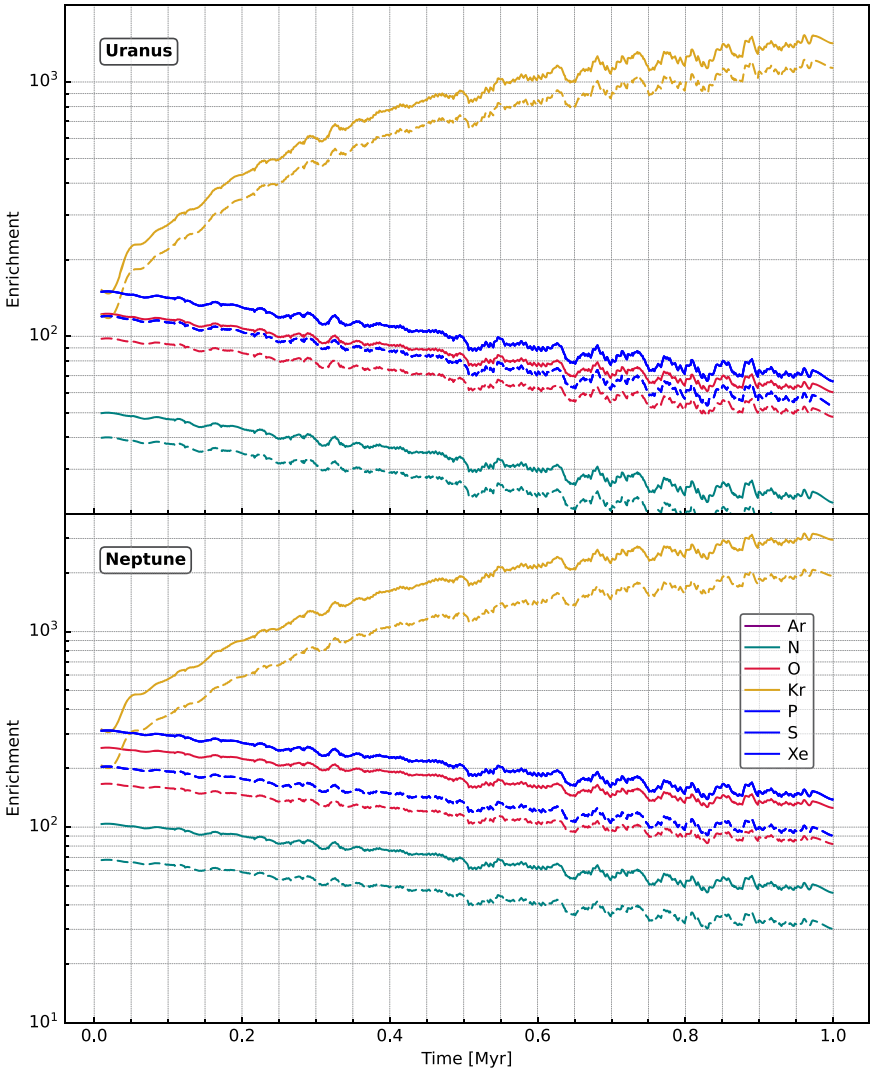

Figure 8. Top panel: elemental enrichments with respect to protosolar abundances predicted in the envelope of Uranus in Case 1, assuming a C enrichment ranging between 40 and 50 times the protosolar value. Dashed and solid lines correspond to predictions of the lower and upper values for the elemental enrichments, respectively. Bottom panel: same as the top panel, but for Neptune, assuming a C enrichment ranging between 68 and 104 times the protosolar value.

to the calibration of their abundances to the higher measured carbon enrichment in Neptune's atmosphere.

Assuming that the heavy elements present in Uranus's envelope were supplied solely by solids formed in the PSN at 0.5 Myr (or 1 Myr) of evolution, the model predicts the following enrichment or impoverishment in volatiles in Case 2:

1. Ar, N, O, and Kr are enriched by factors of 44.0–55.0 (27.4–34.3), 62.3–77.8 (56.2–70.3), 53.0–66.2 (47.7–59.6), and 323.8–404.7 (389.2–486.6), respectively, with respect to their protosolar values.
2. P, S, and Xe are all enriched by a similar factor of 59.0–73.7 (52.6–65.8), with respect to their protosolar values.

Clathrates of various volatile species form at locations closer than the respective ice lines of their pure condensates. This alters the predicted volatile enrichments in Uranus compared to the simple Case 1 scenario of pure condensates only. A key difference is the presence of Ar clathrates at the CO ice line. This engenders a supersolar Ar/C ratio at that location, contrasting with the significant Ar depletion noted in Case 1 due to the lack of an Ar solid reservoir in the PSN. Similar remarks regarding the role of clathrates in trapping volatiles can be formulated for the volatile enrichments in Neptune.

5. Discussion and Conclusion

In this work, we have investigated the key compositional tracers that would be associated with the formation of Uranus and Neptune along the CO ice line in the PSN, assuming that the composition of their building blocks was shaped by the radial transport of particles, dust, and vapors in the disk. A protoplanetary disk and transport model has been used to study the evolution of volatile species throughout the PSN and predict the bulk compositions of Uranus and Neptune. The model tracks the condensation/sublimation of pure condensates and formation of clathrates for different volatile species. Our determination is based on the principle that the heavy elements found in the planetary envelopes were essentially supplied by these solids during the accretion phase and/or by subsequent core erosion. The composition of the solids mirrors that of the grains that crystallized within the planets' feeding

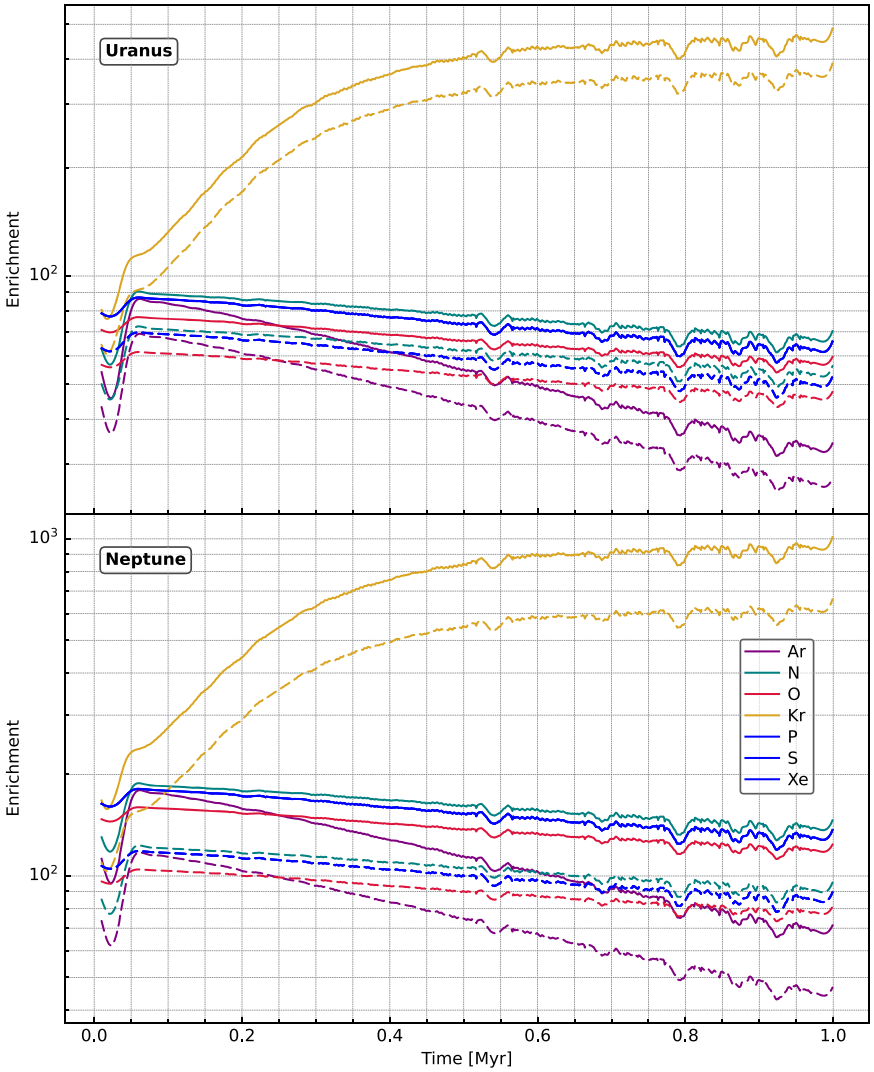

Figure 9. Same as Figure 8, but for Case 2.

zones in the PSN. Two cases have been considered in our simulations: Case 1 assumes that the solids evolving in the PSN were only formed from pure condensates, and Case 2 assumes that these solids could consist of condensates, clathrates, or both. The abundances of the various volatile species in gas, pure condensate, and clathrate forms are calculated as a function of time and heliocentric distance with our disk model.

Both Case 1 and Case 2 predict significant enrichments for most species in the envelopes of Uranus and Neptune. However, the key difference between the two cases is the inclusion of clathrates in Case 2, which significantly affects the predicted Ar abundance. Whereas Case 1 predicts a significant depletion of this noble gas in the envelopes due to its absence in the solids accreted by the two planets, in Case 2 significant amounts of Ar should be trapped in the clathrates that participate in the composition of the solids considered. As a result, supersolar enrichments of Ar are predicted in the envelopes of Uranus and Neptune (see Table 2). Interestingly, the predictions of our model are not very sensitive to the formation epoch of the two ice giants. Although the predicted volatile abundances of solids formed at 1 Myr of PSN evolution are slightly different from the 0.5 Myr case, they remain close.

Any variation in the formation sequence of Uranus and Neptune does not affect the calculations of the composition of the accreted bodies, provided that both planets formed at the CO ice line. However, if one of these planets accreted its heavy elements beyond or below the CO ice line, it would be more challenging to explain the observed carbon enrichment in its atmosphere. This is because the ratio of carbon to hydrogen is higher in solids formed in this region of the PSN, as shown in Figure 3. However, our approach is consistent with planets migrating inward once they have accreted the majority of their heavy elements.

While future in situ measurements promise to refine our understanding of the locations and timing of the formation of the two planets, current uncertainty in carbon measurements used in our model is significant. The error bars associated with these measurements are too wide to effectively explore potentially different chemical pathways between the two planets.

The various elements that are carried by condensible species can only be measured below their respective cloud decks. Following the cloud vertical structure presented in Atreya et al. (2020), C, S and N, and finally O would then require a probe to reach a pressure level of ∼2 bars, 30–50 bars, and several

Table 2
Volatile Enrichments Predicted in Uranus and Neptune at 0.5 and 1 Myr of PSN Evolution

Case	Epoch	Value	Ar	N	O	Kr	P	S	Xe
					Uranus				
Case 1	0.5 Myr	Min	0.0	26.2	67.2	729.7	78.7	78.7	78.7
		Max	0.0	32.8	84.0	912.2	98.4	98.4	98.4
	1 Myr	Min	0.0	17.7	48.2	1135.9	53.2	53.2	53.2
		Max	0.0	22.2	60.3	1419.8	66.6	66.6	66.6
					Neptune				
	0.5 Myr	Min	0.0	44.6	114.3	1240.6	133.8	133.8	133.8
		Max	0.0	68.2	174.8	1897.3	204.6	204.6	204.6
	1 Myr	Min	0.0	30.2	82.0	1931.0	90.5	90.5	90.5
		Max	0.0	46.1	125.4	2953.3	138.4	138.4	138.4
					Uranus				
Case 2	0.5 Myr	Min	44.0	62.3	53.0	323.8	59.0	59.0	59.0
		Max	55.0	77.8	66.2	404.7	73.7	73.7	73.7
	1 Myr	Min	27.4	56.2	47.7	389.2	52.6	52.6	52.6
		Max	34.3	70.3	59.6	486.6	65.8	65.8	65.8
					Neptune				
	0.5 Myr	Min	74.7	105.8	90.0	550.4	100.3	100.3	100.3
		Max	114.3	161.9	137.7	841.8	153.3	153.3	153.3
	1 Myr	Min	46.7	95.6	81.0	661.7	89.4	89.4	89.4
		Max	71.4	146.2	123.0	1012.0	136.8	136.8	136.8

hundred bars, respectively. Because of these important depths, it is desirable that a probe be able to measure secondary carrier species that do not condensate to probe these elements. Measurements of the abundances of species such as CO and N_2 for oxygen and nitrogen require the support of thermochemical models to constrain their deep abundances (Cavalié et al. 2020). In the context of probe measurements, the prediction of the Ar/Kr or Ar/Xe abundance ratios is useful for the assessment of our model because, so far, there is no known differentiation mechanism between these noble gases as long as they remain in the vapor phase. Case 1 predicts that the Ar/Kr or Ar/Xe ratios in Uranus and Neptune are close to zero, while in Case 2 they should be on the order of 0.1 and 0.5–1 times their protosolar ratios in the two planets, respectively. In particular, Xe stands out as the only heavy noble gas capable of condensing in the atmosphere of Uranus, although its cloud level is expected to be in the range of about 0.1–0.4 bars (Zahnle 2023). However, an entry probe would penetrate below this altitude and reach the layer where the noble gases are thoroughly mixed. Measuring the noble gases in situ would be key to testing our various scenarios, since their abundance ratios would in principle not be affected by any possible compositional heterogeneity, as measured in Jupiter by the Juno mission (Helled & Fortney 2020; Bailey & Stevenson 2021).

Assuming that our calculations are representative of homogeneous interiors, the derived O/H ratio is in agreement with the values obtained in Uranus from the thermochemical model of Cavalié et al. (2017) and Venot et al. (2020). At Neptune, the O/H is nominally lower than the model results derived from tropospheric CO observations (Moreno et al. 2017). However, to what extent this value should be considered as an upper limit for the deep neptunian O/H remains debated, as the tropospheric abundance of CO could be much lower than previously thought (Teanby et al. 2019). New broadband and high spectral resolution observations of CO in Neptune are crucially required. The current upper limit for PH_3 stands at 1.1 ppb, as reported by Teanby et al. (2019), established within pressure ranges of 0.1–1.2 bars, a zone where this compound experiences significant photochemical loss. It is thus not possible to use this observation as a constraint for comparison with the P/H value resulting from our simulations. The fact that our model predicts more PH_3 than the upper limit set by Teanby et al. (2019) confirms the photochemical losses in the upper troposphere. Beyond 0.5 Myr of simulation, we obtain a sulfur-to-nitrogen ratio of ∼15 in Case 1 and ∼5 in Case 2. This is in agreement with the measurements of Irwin et al. (2018) and Irwin et al. (2019), who find that sulfur-to-nitrogen ratio exceeds unity in Uranus and Neptune. Their detection of H_2S at pressures of a few bars suggests a prevalence of H_2S over NH_3, as indicated by the survival of some H_2S after the formation of NH_4SH clouds at depths of 30–50 bars.

It is important to note that the positions of ice lines in our model are contingent on the PSN temperature/pressure profiles, which themselves rely on a number of factors, including solar irradiation, the chosen viscosity parameter, disk opacity, and others. Consequently, it is crucial to acknowledge the inherent variability in determining the precise locations of ice lines. Models that posit the formation of ice giants at greater heliocentric distances, such as within the 12–17 au range (Tsiganis et al. 2005), do not inherently contradict our findings in this regard.

It is also notable that the formation lines for clathrates are situated closer to the Sun compared to the CO ice line. Consequently, the impact of this solid reservoir is reduced at the location of the ice giants, which are assumed to form at the CO ice line within the PSN. If we consider the possibility that Jupiter and Saturn formed from pebbles at heliocentric distances closer to the Sun, the significance of clathrates in their formation processes could be enhanced. This possibility warrants further investigation in the future.

Acknowledgments

This research holds as part of the project FACOM (ANR-22-CE49-0005-01_ACT) and has benefited from a funding provided by l'Agence Nationale de la Recherche (ANR) under

the Generic Call for Proposals 2022. The project leading to this publication has received funding from the Excellence Initiative of Aix-Marseille Université–A*Midex, a French "Investissements d'Avenir program" AMX-21-IET-018. O.M. and T.C. acknowledge funding from CNES. V.H. acknowledges support from the French government under the France 2030 investment plan, as part of the Initiative d'Excellence d'Aix-Marseille Université—A*MIDEX AMX-22-CPJ-04. K.E.M. acknowledges support from NASA RDAP grant 80NSSC19K1306. J.I.L. was funded for this study as the David Baltimore Distinguished Visiting Scientist at JPL.

ORCID iDs

Olivier Mousis https://orcid.org/0000-0001-5323-6453
Antoine Schneeberger https://orcid.org/0000-0002-3289-2432
Thibault Cavalié https://orcid.org/0000-0002-0649-1192
Kathleen E. Mandt https://orcid.org/0000-0001-8397-3315
Artyom Aguichine https://orcid.org/0000-0002-8949-5956
Jonathan I. Lunine https://orcid.org/0000-0003-2279-4131
Tom Benest Couzinou https://orcid.org/0000-0002-8719-7867
Vincent Hue https://orcid.org/0000-0001-9275-0156
Raphaël Moreno https://orcid.org/0000-0002-9171-2702

References

Aguichine, A., Mousis, O., Devouard, B., et al. 2020, ApJ, 901, 97
Ali-Dib, M., Mousis, O., Petit, J.-M., et al. 2014, ApJ, 793, 9
Atreya, S. K., Hofstadter, M. H., In, J. H., et al. 2020, SSRv, 216, 18
Bailey, E., & Stevenson, D. J. 2021, PSJ, 2, 64
Balsiger, H., Altwegg, K., Bar-Nun, A., et al. 2015, SciA, 1, e1500377
Bell, K. R., & Lin, D. N. C. 1994, ApJ, 427, 987
Bergin, E. A., Blake, G. A., Ciesla, F., et al. 2015, PNAS, 112, 8965
Birnstiel, T., Klahr, H., & Ercolano, B. 2012, A&A, 539, A148
Bosman, A. D., Cridland, A. J., & Miguel, Y. 2019, A&A, 632, L11
Burgdorf, M., Orton, G. S., Davis, G. R., et al. 2003, Icar, 164, 244
Cavalié, T., Moreno, R., Lellouch, E., et al. 2014, A&A, 562, A33
Cavalié, T., Venot, O., Miguel, Y., et al. 2020, SSRv, 216, 58
Cavalié, T., Venot, O., Selsis, F., et al. 2017, Icar, 291, 1
Conrath, B., Gautier, D., Hanel, R., et al. 1987, JGR, 92, 15003
Deleuil, M., Pollacco, D., Baruteau, C., et al. 2020, SSRv, 216, 105
Desch, S. J., Estrada, P. R., Kalyaan, A., et al. 2017, ApJ, 840, 86
Drażkowska, J., & Alibert, Y. 2017, A&A, 608, A92
Fegley, B. J. 2000, SSRv, 92, 177
Feuchtgruber, H., Lellouch, E., Orton, G., et al. 2013, A&A, 551, A126
Fletcher, L. N., de Pater, I., Orton, G. S., et al. 2014, Icar, 231, 146
Fletcher, L. N., Drossart, P., Burgdorf, M., et al. 2010, A&A, 514, A17
Hartmann, L., Calvet, N., Gullbring, E., et al. 1998, ApJ, 495, 385
Helled, R., & Fortney, J. J. 2020, RSPTA, 378, 20190474
Hueso, R., & Guillot, T. 2005, A&A, 442, 703
Irwin, P. G. J., Dobinson, J., James, A., et al. 2021, Icar, 357, 114277
Irwin, P. G. J., Toledo, D., Braude, A. S., et al. 2019, Icar, 331, 69
Irwin, P. G. J., Toledo, D., Garland, R., et al. 2018, NatAs, 2, 420
Johansen, A., Blum, J., Tanaka, H., et al. 2014, in Protostars and Planets VI, ed. H. Beuther et al. (Tucson, AZ: Univ. Arizona Press), 547
Karkoschka, E., & Tomasko, M. 2009, Icar, 202, 287
Karkoschka, E., & Tomasko, M. G. 2011, Icar, 211, 780
Lambrechts, M., & Johansen, A. 2014, A&A, 572, A107
Lambrechts, M., Johansen, A., & Morbidelli, A. 2014, A&A, 572, A35
Le Roy, L., Altwegg, K., Balsiger, H., et al. 2015, A&A, 583, A1
Lellouch, E., Moreno, R., Orton, G. S., et al. 2015, A&A, 579, A121
Lindal, G. F. 1992, AJ, 103, 967
Lindal, G. F., Lyons, J. R., Sweetnam, D. N., et al. 1987, JGR, 92, 14987
Lodders, K. 2021, SSRv, 217, 44
Lynden-Bell, D., & Pringle, J. E. 1974, MNRAS, 168, 603
Moreno, R., Lellouch, E., Cavalié, T., et al. 2017, A&A, 608, L5
Mousis, O., Aguichine, A., Helled, R., et al. 2020, RSPTA, 378, 20200107
Mousis, O., Atkinson, D. H., Ambrosi, R., et al. 2022, ExA, 54, 975
Mousis, O., Lunine, J. I., Fletcher, L. N., et al. 2014, ApJL, 796, L28
Mousis, O., Lunine, J. I., Thomas, C., et al. 2009, ApJ, 691, 1780
Nakamoto, T., & Nakagawa, Y. 1994, ApJ, 421, 640
Öberg, K. I., & Wordsworth, R. 2019, AJ, 158, 194
Ohno, K., & Ueda, T. 2021, A&A, 651, L2
Orton, G. S., Fletcher, L. N., Moses, J. I., et al. 2014a, Icar, 243, 494
Orton, G. S., Moses, J. I., Fletcher, L. N., et al. 2014b, Icar, 243, 471
Pasek, M. A., Milsom, J. A., Ciesla, F. J., et al. 2005, Icar, 175, 1
Rucska, J. J., & Wadsley, J. W. 2023, MNRAS, 526, 1757
Schneeberger, A., Mousis, O., Aguichine, A., et al. 2023, A&A, 670, A28
Shakura, N. I., & Sunyaev, R. A. 1973, in Proc. of IAU Symp. 55, X- and Gamma-Ray Astronomy, ed. H. Bradt & R. Giacconi (Dordrecht: Reidel), 155
Smith, B. A., Soderblom, L. A., Banfield, D., et al. 1989, Sci, 246, 1422
Smith, B. A., Soderblom, L. A., Beebe, R., et al. 1986, Sci, 233, 43
Sromovsky, L. A., Karkoschka, E., Fry, P. M., et al. 2014, Icar, 238, 137
Sromovsky, L. A., Karkoschka, E., Fry, P. M., et al. 2019, Icar, 317, 266
Stone, E. C., & Miner, E. D. 1989, Sci, 246, 1417
Teanby, N. A., Gould, B., & Irwin, P. G. J. 2021, Icar, 354, 114045
Teanby, N. A., & Irwin, P. G. J. 2013, ApJL, 775, L49
Teanby, N. A., Irwin, P. G. J., & Moses, J. I. 2019, Icar, 319, 86
Teanby, N. A., Irwin, P. G. J., Sylvestre, M., et al. 2022, PSJ, 3, 96
Tsiganis, K., Gomes, R., Morbidelli, A., et al. 2005, Natur, 435, 459
Tyler, G. L., Sweetnam, D. N., Anderson, J. D., et al. 1986, Sci, 233, 79
Venot, O., Cavalié, T., Bounaceur, R., et al. 2020, A&A, 634, A78
Weidenschilling, S. J. 1997, Icar, 127, 290
Williams, J. P., & Cieza, L. A. 2011, ARA&A, 49, 67
Zahnle, K. J. 2023, Uranus Flagship: Investigations and Instruments for Cross-Discipline Science Workshop, 2808, 8068